Tellus (1997), 49A, 559–576
Printed in UK – all rights reserved

TELLUS
ISSN 0280–6495

The dynamics of cold fronts passing over a quasi-two-dimensional mountain ridge

By JINXING ZONG[1] and QIN XU*[2], [1]Center for Analysis and Prediction of Storms, University of Oklahoma, 100 E. Boyd, Norman, OK 73019-0628, USA; [2]Naval Research Laboratory, 7 Grace Hopper Drive, Monterey, CA 93943-5502, USA.

(Manuscript received 29 April 1996; in final form 8 July 1997)

ABSTRACT

A two-layer semigeostrophic model is developed for cold fronts passing over a quasi-two-dimensional mesoscale mountain ridge oriented north-south. A constant potential vorticity is assumed for the cold air in the lower layer, while a steady-state geostrophic flow is specified in the upper layer. A hyperbolic differential equation is derived for the movement of the surface cold front. As long as the topographic slope is not as steep as the frontal slope on the lee side of the mountain, this equation remains valid and can be integrated by following the characteristic velocity which is expressed analytically in terms of the frontal position and the topography underlying the cold air. Solutions are obtained for two cases of different upper-layer geostrophic wind: southwesterly in case 1, and northwesterly in case 2. The topographic effects on the frontal evolution are examined in detail from a kinematic viewpoint in connection with the characteristic velocity and from a dynamic viewpoint in connection with the geostrophic and ageostrophic components of the perturbation wind field in the cold air. It is shown that the frontal evolution can be roughly divided into two stages: the upslope stage and the downslope stage. During the upslope stage, the surface front moves on the upstream side of the mountain, the cold air layer becomes shallower over the mountain, and the perturbation geostrophic flow is curved anticyclonically under the constraint of potential vorticity conservation. During the downslope stage, the surface front moves on the lee side of the mountain, the front becomes steep, and the perturbation geostrophic flow becomes strong and fairly parallel to the distorted front. As the frontal-wave propagates further downstream, leaving behind an anticyclone associated permanently with the topography, the transient and long-term effects of the topography on the flow field are essentially decoupled. Noticeable differences in the frontal evolution between the two cases are revealed.

1. Introduction

In recent years, much research has focused on issues related to front movement over complex terrain. Observations of cold fronts passing the Alps have been analyzed by many authors (Buzzi and Tibaldi, 1978; Steinacker, 1981, 1983; Davies, 1986; Hoinka, 1986). More recently, Hoinka and Heimann (1988) described the channeling effect of the Pyrenees on a cold front using high resolution surface data, and showed that the surface front is trapped significantly in the vicinity of the mountains. In addition, the southerly buster, a unique phenomenon in the coastal regions of south eastern Australia, seems to be associated with the deformation of a cold front interacting with local mountains (Baines, 1980; Colquhoun et al., 1985; Garratt et al., 1989).

There have also been considerable theoretical and numerical studies concerning topographic effects on cold fronts (Bannon, 1984; Davies, 1984;

* Corresponding author.
e-mail: XUQ@nrlmry.navy.mil

Schumann, 1987; Williams et al., 1992; Gu and Wu, 1992; Egger and Hatt, 1994), although most of these studies have been two-dimensional analyses. In particular, Davies (1984) has obtained an analytical solution of cold front movement over an idealized mountain ridge using a two-dimensional semigeostrophic model on an f-plane. This solution appears to be very useful for understanding the orographic retardation of cold fronts. According to the aforementioned and other observational studies, however, the movements of cold fronts around real mountains often involve three-dimensional features (see also Smith, 1986; and Egger and Hoinka, 1992 for reviews). The three-dimensionality of topography brings certain difficulties to theoretical and numerical analyses. Theoretical studies in this direction have been very limited (Blumen and Gross, 1987; Schumann, 1987; Blumen, 1992), and hence the dynamics of frontal distortion by three-dimensional topography remains only partially understood.

The purpose of this paper is to provide detailed analyses of the effects of quasi-two-dimensional topography on cold front movement in three-dimensional space. For a cold front moving toward an elongated mountain roughly parallel to the front, semigeostrophy can remain valid. This and related conditions allow an analytical treatment of the model's equations, and the derived formulations will be employed to analyze the frontal movement influenced by the topography. Solutions will be obtained for two cases of different upper-layer geostrophic flows: southwesterly and northwesterly. The frontal movement and related topographic effects will be examined for each case from a kinematic viewpoint in connection with the characteristic velocity of the frontal propagation and from a dynamic viewpoint in connection with the geostrophic and ageostrophic components of the perturbation wind in the cold air. Special attention will be given to the along-front structure produced by the interaction between the front and the underlying topography. The paper is organized as follows. The model equations and front configuration are described in the following section. Section 3 derives a hyperbolic partial differential equation that governs the movement of the surface front. Numerical solutions are obtained and examined in Section 4, while analytical solutions of the frontal motion in the absence of topography are derived in the Appendix. Section 5 ends the paper with a summary and discussion.

2. Basic equations and front configuration

Consider two homogeneous layers of fluid of different densities, with the lighter (warmer) fluid lying over the denser (colder) one. The lower-layer fluid approaches a constant depth H far upstream (i.e., $x \to -\infty$), and the cold front is represented by the sloping interface $h = h(x, y, t)$ between the two fluids. The surface front is defined as the line where the frontal interface intersects the underlying topography $h_o = h_o(x, y)$. The upper-layer fluid affects the lower-layer flow through the pressure gradient force and the associated geostrophic wind, denoted by (u_1, v_1), is assumed to be stationary. Initially, the cold front is oriented north-south (along the y-direction in the Cartesian coordinates) and moves with an eastward velocity component $u_1 > 0$ towards an isolated quasi-two-dimensional mountain. The mountain is elongated in the y-direction and is relatively narrow in the x-direction. The horizontal extensions of the mountain can be characterized by two length scales: ℓ in the x-direction and L in the y-direction, with $L \gg \ell$. Here, L is in the synoptic scale range and ℓ is in the subsynoptic or mesoscale range.

The model variables are scaled as follows:

$$x \leftarrow x/\ell, \quad y \leftarrow y/L, \quad t \leftarrow t/(L/V),$$
$$(u, u_1) \leftarrow (u, u_1)/\ell V/L),$$
$$(v, v_1) \leftarrow (v, v_1)/V, \; (h, h_0) \leftarrow (h, h_0)/H,$$

where the variables on the right-hand side of each arrow are dimensional, the variables on the left-hand side are dimensionless and will be used throughout this paper. Here (u, v) is the total velocity field for the cold air in the lower layer, $V \equiv (Hg')^{1/2}$ is the velocity scale for the v-component, $V\ell/L$ is the velocity scale for the u-component, $g' \equiv g\Delta\rho/\rho_0$ is the reduced acceleration of gravity, ρ_0 is the density of the lower-layer fluid, $\Delta\rho$ is the density difference between the two fluids, and f is the constant Coriolis parameter.

Using the above scaling, one can derive a dimensionless system of shallow-water equations for the lower-layer fluid (not shown). This system of equations contains only one small parameter: $(\ell/L)^2$, and this small parameter is associated only with the Lagrangian time derivative term in the u-momentum equation. When this time derivative term is neglected, the truncated leading-order system gives the following semigeostrophic equations (see Hoskins and Bretherton, 1972):

$$v = R\partial h/\partial x + v_1, \tag{2.1}$$

$$R\mathrm{d}v/\mathrm{d}t + u = -R\partial h/\partial y + u_1, \tag{2.2}$$

$$\partial h/\partial t + \partial[(h-h_o)u]/\partial x + \partial[(h-h_o)v]/\partial y = 0, \tag{2.3}$$

where $d(\ )/\mathrm{d}t \equiv \partial(\ )/\partial t + u\partial(\ )\partial x + v\partial(\ )/\partial y$ is the Lagrangian time derivative of ( ) following the total velocity (u, v), and $R \equiv V/(f\ell) \leqslant O(1)$ is the Rossby number. Since the parcel acceleration term is neglected only in (2.1), geostrophic balance is assumed only in the x direction. In comparison with Davies' model (1984), the additional terms retained in our model include the meridional momentum advection and meridional pressure gradient force in (2.2), and the meridional mass convergence term in (2.3). From (2.2) and (2.3), we see that these terms have comparable orders of magnitude to the other terms.

From (2.1)–(2.3), we obtain the following potential vorticity conservation equation:

$$\mathrm{d}q/\mathrm{d}t = 0, \tag{2.4}$$

where $q \equiv (1 + R\partial v/\partial x)/(h-h_o)$ is the potential vorticity for the lower layer flow, that is, the absolute vorticity divided by the depth of the lower layer fluid. Note that another part of the vorticity is related to $-\partial u/\partial y$, and this part is neglected in the expression of q according to the semigeostrophy assumed in the model eqs. (2.1)–(2.3). A direct scale analysis further shows that the ratio between $-\partial u/\partial y$ and $\partial v/\partial x$ is measured by $(\ell/L)^2$, which is much smaller than O(1). As the lower-layer fluid is from far upstream where the potential vorticity is assumed to be unity (scaled by f/H), potential vorticity conservation (2.4) implies the following constraint

$$1 + R\partial v/\partial x = h - h_o, \tag{2.5}$$

which requires the absolute vorticity to be proportional to the depth of the cold air.

Eliminating v between (2.1) and (2.5) we obtain an equation for h:

$$(R^2\partial^2/\partial x^2 - 1)h = -1 - h_o - R\partial v_1/\partial x. \tag{2.6}$$

The solution of (2.6) has the following general form:

$$h = D(x, y) + A(y, t)\,\mathrm{e}^{x/R} + B(y, t)\,\mathrm{e}^{-x/R}, \tag{2.7}$$

where $A(y, t)$ and $B(y, t)$ are integral constants to be determined, and D is the particular solution — a response function to the forcing on the right-hand side of (2.6). Since h_o and v_1 are independent of t, the particular solution is given by

$$D(x, y) = 1 + \left[\int_{-\infty}^{x} (h_o - v_1)\,\mathrm{e}^{(x'-x)/R}\mathrm{d}x' + \int_{x}^{\infty} (h_o + v_1)\,\mathrm{e}^{-(x'-x)/R}\mathrm{d}x'\right]\Big/(2R), \tag{2.8a}$$

which is a bounded function of x and y. When v_1 is constant, this solution reduces to

$$D(x, y) = 1 + \left[\int_{-\infty}^{x} h_o\,\mathrm{e}^{(x'-x)/R}\,\mathrm{d}x' + \int_{x}^{\infty} h_o\,\mathrm{e}^{-(x'-x)/R}\,\mathrm{d}x'\right]\Big/(2R). \tag{2.8b}$$

Physically h is bounded as $x \to -\infty$, and this implies $B = 0$ in (2.7). The interface intersects the ground at the surface front, and this can be expressed by

$$h = h_o \quad \text{at} \quad x = \xi(y, t), \tag{2.9}$$

where $\xi(y, t)$ denotes the surface frontal position in the x-coordinate. Substituting (2.9) into (2.7) with $B = 0$ determines the other integral constant A and thus the general form of solution in (2.7) reduces to

$$h = D(x, y) + [h_o - D]_\xi\,\mathrm{e}^{(x-\xi)/R}, \tag{2.10}$$

where the subscript ξ indicates that the value in the parentheses is evaluated at $x = \xi$ — the position of the surface front. This convention for the subscript ξ is adopted throughout the paper. As shown in (2.10), the structure of the frontal interface is described by two parts: a steady part D associated with the mountain, and a transient part that translates with the surface front and decays exponentially away from the surface front.

Differentiating (2.10) with respect to t gives:

$$\partial h/\partial t=[\partial(h_o-D)/\partial x-(h_o-D)/R]_\xi(\partial\xi/\partial t)\,e^{(x-\xi)/R}. \tag{2.11}$$

This shows that $\partial h/\partial t$ is proportional to $\partial\xi/\partial t$ and the transient behaviors of h and ξ are interrelated. Note that the transient variation of h vanishes as $(x-\xi)/R\to-\infty$. This implies that the transient part of h is primarily confined to the vicinity of the surface front within the Rossby radius of deformation scaled by ℓ. (Note that $R=V/(f\ell)=(Hg')^{1/2}/(f\ell)$.) Away from this vicinity, h is described by D. Since the function $\xi(y,\ t)$ is unknown in (2.10), we need to derive the governing equation for ξ in Section 3.

3. Equations governing cold front movement

3.1. Characteristic equations

In the previous section, the frontal interface h is expressed in terms of $(\xi,\ h_o)$ in (2.10). By substituting this expression into (2.1) and (2.2), we can obtain expressions for u and v in terms of $(\xi,\ h_o)$. Further substituting these expressions with the time derivative of h in (2.11) into (2.3), we can derive a single hyperbolic equation that describes the evolution of the surface frontal position ξ. The derivation can be done in many ways. The most convenient way that we found involves a few intermediate steps, and the details are presented as follows.

By using (2.5), the momentum eq. (2.2) can be rearranged into the following form

$$R\partial v/\partial t=u_1-(h-h_o)u-R\partial E/\partial y, \tag{3.1}$$

where

$$E=h+v^2/2 \tag{3.2}$$

is the semigeostrophic Bernoulli energy for the lower-layer flow. Eliminating h from (2.1) and (2.5), we obtain

$$(R^2\partial^2/\partial x^2-1)v=-v_1-R\partial h_o/\partial x. \tag{3.3}$$

Substituting (3.1) into the time derivative of (3.3) gives

$$(R^2\partial^2/\partial x^2-1)[(h-h_o)u-u_1+R\partial E/\partial y]=0. \tag{3.4}$$

The solution of (3.4), that is bounded as $x\to-\infty$, has the following form

$$(h-h_o)u=u_1-R\partial E/\partial y-[u_1-R\partial E/\partial y]_\xi\, e^{(x-\xi)/R}. \tag{3.5}$$

This result can be used for the second term in the continuity eq. (2.3).

The expression for the last term in the continuity eq. (2.3) can be derived as follows by using (2.5) and rearranging the momentum eq. (2.1):

$$(h-h_o)v=v_1+R\partial E/\partial x. \tag{3.6}$$

Substituting (2.11), (3.5) and (3.6) into the continuity eq. (2.3) gives

$$[\partial(h_o-D)/\partial x-(h_o-D)/R]_\xi(\partial\xi/\partial t)=[u_1/R-\partial E/\partial y]_\xi. \tag{3.7}$$

By using (2.1), (2.10) and (3.2), $[\partial E/\partial y]_\xi$ can be expressed in terms of $(\xi,\ h_o)$. Substituting this expression into (3.7) yields the following governing equation for ξ:

$$\partial\xi/\partial t+v_o\partial\xi/\partial y=u_o, \tag{3.8}$$

where v_o and u_o are defined by

$$v_o=[1+v_2]_\xi, \tag{3.9a}$$

$$u_o=[u_1-R\partial h_o/\partial y-Rv_2\partial v_2/\partial y]_\xi/C, \tag{3.10a}$$

$$C=[R\partial(h_o-D)/\partial x-(h_o-D)]_\xi. \tag{3.11a}$$

where $v_2\equiv v_1+R\partial D/\partial x-D+h_o$ and D is given by (2.8a). If the upper-layer wind $(u_1,\ v_1)$ is a constant vector, D is given by (2.8b), and eqs. (3.9a)–(3.11a) reduce to

$$v_o=v_1+\int_{-\infty}^{\xi}(\partial h_o/\partial x)e^{(x-\xi)/R}\,dx, \tag{3.9b}$$

$$u_o=\left[u_1-R(\partial h_o/\partial y)_\xi+R(1-v_o)\times\int_{-\infty}^{\xi}(\partial^2 h_o/\partial x\partial y)e^{(x-\xi)/R}\,dx\right]\Big/C, \tag{3.10b}$$

$$C=1+R\int_{-\infty}^{\xi}(\partial^2 h_o/\partial x^2)e^{(x-\xi)/R}\,dx. \tag{3.11b}$$

Note that (3.8) is a hyperbolic partial differential equation, and its characteristic velocity (u_o, v_o) is given as a known function of (ξ, y) in (3.9)–(3.11). The related initial value problem can be solved by integrating the associated characteristic equations:

$$d_o\xi/dt = u_o(\xi, y), \tag{3.12a}$$

$$d_o y/dt = v_o(\xi, y), \tag{3.12b}$$

where $d_o(\ )/dt$ denotes the ordinary time differentiation of ( ). When (3.12) is integrated forward in time, the solution (ξ, y) describes how the surface front moves following the characteristic velocity (u_o, v_o). In this paper, the initial surface front is assumed to be a straight line along the y-direction far upstream to the west of the mountain (although in general the initial surface front can be curved as shown in the Appendix). The high-accuracy Runge-Kutta method will be employed to integrate (3.12a,b) with the characteristic velocity (u_o, v_o) given by (3.10b) and (3.9b).

3.2. *Characteristic velocity and parcel velocity at the surface front*

Now we examine how the characteristic velocity (u_o, v_o) is related to the parcel velocity on the surface front. Since there is no internal vertical circulation within the lower-layer fluid in this model, the surface front is a material line described by $x=\xi(y, t)$ or, equivalently, by $(h-h_o)_\xi=0$. The surface frontal movement satisfies the following Lagrangian equation:

$$u = dx/dt = \partial\xi/\partial t + v\partial\xi/\partial y$$

$$\textit{following parcels on } x=\xi(y, t), \tag{3.13a}$$

or

$$d(h-h_o)/dt=0$$

$$\textit{following parcels on } (h-h_o)_\xi=0, \tag{3.13b}$$

where $d(\ )/dt$ is the Lagrangian time derivative of ( ) as defined in (2.2), and the subscript ξ implies $x=\xi$. By substituting (2.10) into (2.1) and using (3.5) and (2.10), v and u can be expressed in terms of ξ and (x, y, t). By setting $x=\xi(y, t)$ in these expressions, we obtain

$$v(\xi, y, t) = v_o - 1, \tag{3.14a}$$

$$u(\xi, y, t) = u_o - \partial\xi/\partial y, \tag{3.14b}$$

where (u_o, v_o) is the characteristic velocity given by (3.9)–(3.11). Note that the vector difference $(u_o, v_o) - [u(\xi, y, t), v(\xi, y, t)] = [\partial\xi/\partial y, 1]$ is tangential to the surface frontal line: $x=\xi(y, t)$, so the characteristic velocity (u_o, v_o) is not the frontal parcel velocity but is the sum of the frontal parcel velocity and an along-frontal vector $(\partial\xi/\partial y, 1)$.

The model breaks down under a certain condition. To see this, we need to derive the following relationships. By using (2.10), we obtain:

$$[\partial(h-h_o)/\partial x]_\xi = -[\partial(h_o-D)/\partial x - (h_o-D)/R]_\xi$$
$$= -C/R, \tag{3.15}$$

where C is given in (3.11). This result shows that the relative slope of the surface front with respect to the topography in the x-direction is given by $-C/R$ in the dimensionless space. Substituting (3.15) into (2.11) at $x=\xi$ gives

$$[\partial(h-h_o)\partial t]_\xi = -[\partial(h-h_o)/\partial x]_\xi \partial\xi/\partial t$$
$$= (C/R)\partial\xi/\partial t. \tag{3.16}$$

Similarly, by using (2.10) and differentiating $h-h_o$ with respect to y, we obtain:

$$[\partial(h-h_o)/\partial y]_\xi = -[\partial(h-h_o)/\partial x]_\xi \partial\xi/\partial y$$
$$= (C/R)\partial\xi/\partial y. \tag{3.17}$$

According to (3.10a), (3.14b) and (3.15), $u_o\to\infty$ and thus $[u]_\xi\to\infty$ as $R[\partial(h-h_o)\partial x]_\xi = -C\to 0$ or, say, as the relative slope of the front becomes zero with respect to the topography in the x-direction. This implies that the surface front propagates in the x-direction with an unbounded speed, that is, $\partial\xi/\partial t\to\infty$ as $C\to 0$, but $[\partial(h-h_o)/\partial x]_\xi\partial\xi/\partial t$ and $[\partial(h-h_o)/\partial t]_\xi$ can remain finite in (3.16). Thus, $C=0$ is a breakdown condition for the semigeostrophic model in this paper, and this condition is similar to that in the two-dimensional model of Davies (1984). The assumed quasi-two-dimensionality and related semigeostrophy require that the surface front not be distorted dramatically from the y-direction. At least, $|\partial\xi/\partial y|<\infty$ is required as $C\to 0$. Substituting this into (3.17) gives $[\partial(h-h_o)/\partial y]_\xi\to 0$, as $C\to 0$, so the surface front must be along the y-direction as $C\to 0$. This feature is seen in our model's solution, and it ensures the validity of the quasi-two-dimensional semigeostrophy used in this paper.

4. Numerical results and discussions

For a quantitative analysis, the following Gaussian-type mountain profile is adopted:

$$h_o(x, y) = \gamma \hat{h}_o(x, y) = \gamma \exp[-(x^2+y^2)], \quad (4.1)$$

where γ is the dimensionless mountain height (scaled by H— the far-upstream depth of the lower-layer cold air); $\hat{h}_o(x, y)$ represents the Gaussian-type profile. Note that the x-coordinate is scaled by ℓ, while the y-coordinate is scaled by L, so the e-folding height contour of the mountain in the dimensional space is an elongated ellipse with its short axis equal to 2 ℓ in the x-direction and its long axis equal to $2L$ in the y-direction. The upper-layer geostrophic wind (u_1, v_1) is also scaled anisotropically (as shown in Section 2) and is assumed to be constant in this section.

Because of the semigeostrophic approximation used in the model, the dimensionless mountain height γ is restricted above by a critical value γ_c (which is a function of the Rossby number as shown in Fig. 1). When γ reaches this critical value, the topographic slope becomes as steep as the frontal slope on the lee side of the mountain and the frontal movement speed becomes locally unbounded (implying a strong downslope wind beyond the description of the present model). As a result, the model breaks down. The breakdown condition will be derived in the following subsection. Then, solutions will be obtained for two cases of different upper-layer geostrophic winds with a specified mountain height $\gamma < \gamma_c$. The frontal evolution and related topographic modification in each case will be examined both from a kinematic viewpoint in Subsection 4.2 and from a dynamic viewpoint in Subsection 4.3. As will be seen in these subsections, the frontal evolution can be roughly divided into 2 stages: the upslope stage and the downslope stage. During the upslope stage, the surface front moves on the upstream side of the mountain, and the transient and long-term effects of the topography on the flow field are closely coupled as a result of the interaction between the front and topography. During the downslope stage, the surface front moves on the lee side of the mountain. As the frontal-wave propagates downstream, leaving behind an anticyclone permanently associated with the topography, the transient and long-term effects of the topography on the flow field are decoupled.

4.1. Breakdown condition

From the frontal configuration defined in the preceding sections we have $\partial h/\partial x < 0$. Furthermore, $\partial h_o/\partial x > 0$ on the west side and $\partial h_o/\partial x < 0$ on the east side of the mountain. Therefore, the breakdown condition ($C=0$) can only occur on the east side where $\partial h/\partial x$ and $\partial h_o/\partial x$ have the same sign. In order to quantify how the breakdown condition is related to the mountain height γ, we need to examine the minimum of $C = 1 + C_o$, where

$$C_o = R \int_{-\infty}^{\xi} (\partial^2 h_o/\partial x^2)\, e^{(x-\xi)/R}\, dx \quad (4.2)$$

is the 2nd term in (3.11b). Since h_o in (4.1) is separable in x and y, the minimum of C_o occurs on $y=0$ and, thus, we only need to examine the behavior of C_o with respect to ξ along $y=0$.

Differentiating (4.2) with respect to ξ gives

$$\partial C_o/\partial \xi + C_o/R = R\partial^2 h_o/\partial \xi^2 . \quad (4.3)$$

The right-hand-side forcing $R\partial^2 h_o/\partial \xi^2$ in (4.3) is oscillatory with respect to ξ with a negative minimum at $\xi=0$, and the solution C_o has a similar but shifted oscillatory pattern (not shown). At the minimum point of C_o, $\partial C_o/\partial \xi = 0$, and hence (4.3) reduces to

$$[C_o]_{\xi_c} = R^2[\partial^2 h_o/\partial \xi^2]_{\xi_c}, \quad (4.4)$$

where ξ_c denotes the minimum point of C_o. Since $[C_o]_{\xi_c} < 0$, (4.4) suggests that

$$[\partial^2 h_o/\partial \xi^2]_{\xi c} < 0 . \quad (4.5)$$

By using (4.1) and (4.4), the minimum of C is given by $[C]_{\xi c} = 1 + [C_o]_{\xi c} = 1 + R^2[\partial^2 h_o/\partial \xi^2]_{\xi c} = 1 + \gamma R^2[\partial^2 \hat{h}_o/\partial \xi^2]_{\xi c} = 0$. Setting $[C]_{\xi c} = 0$ gives the critical value of γ:

$$\gamma_c = -R^{-2}/[\partial^2 \hat{h}_o/\partial \xi^2]_{\xi c}, \quad (4.6)$$

which is positive due to (4.5). When $\gamma < \gamma_c$, $C > 0$ and there is no breakdown. Note that ξ_c can be determined as a function of R from (4.4) and (4.2), so $-[\partial^2 \hat{h}_o/\partial \xi^2]_{\xi c} = (R^2\gamma_c)^{-1}$ can be calculated as a function of R^{-1} and the result is plotted in Fig. 1. As shown, $(R^2\gamma_c)^{-1} \to 2$ when $R^{-1} \to \infty$, so $\gamma_c \to 1/(2R^2)$ in the limit of infinitely strong rotation ($R \to 0$). Note that the vertical and horizontal coordinates have different scales in Fig. 1 and the dotted straight line is the 1:1 diagonal, so $(R^2\gamma_c)^{-1} \to R^{-1}$ as $R \to \infty$. Therefore, $\gamma_c \to R^{-1} \to 0$ in the limit of infinitely weak rotation ($R \to \infty$).

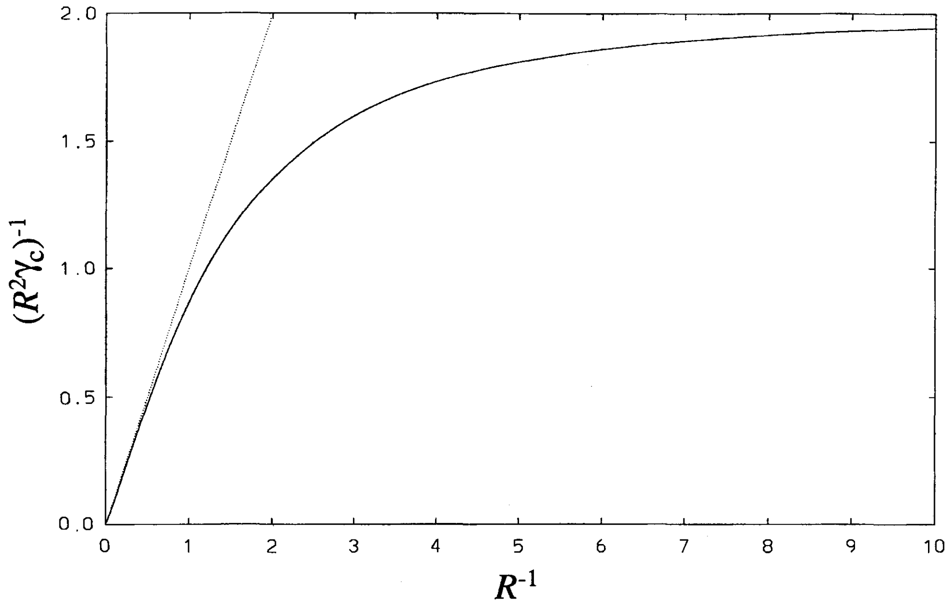

Fig. 1. Variation of $-[\partial^2\hat{h}_o/\partial\xi^2]_{\xi_c}=(R^2\gamma_c)^{-1}$ as a function of R^{-1}. The dotted straight line is the 1:1 diagonal.

The overall quantitative results obtained in this subsection are similar to those of Davies (1984), but (4.6) and the related formulations allow the breakdown condition to be examined in a broader range of the parameters involved.

With the Gaussian-type mountain profile given in (4.1), the dimensionless flow is controlled by four external parameters: the Rossby number R, the dimensionless mountain height γ, and the two components of the upper-layer geostrophic velocity (u_1, v_1). The model solution remains valid as long as γ is below the critical value γ_c. As shown in (4.6) and Fig. 1, the critical value γ_c increases monotonically with R^{-1} and is independent of (u_1, v_1). When $R=1$ is chosen for a mesoscale mountain, $\gamma_c=1.1515$ is obtained from (4.1) and (4.6). In the following subsections, solutions are obtained and examined for $R=1$, $\gamma=0.5$ $(<\gamma_c)$ and different (u_1, v_1).

4.2. *Frontal movement and topographic modification of the front*

The analytical formulations derived for the characteristic velocity in (3.9)–(3.11) are used in this section to interpret the computed frontal movements and to analyze the asymptotic behaviors of the solutions in the limit of small Rossby number. In particular, the frontal movement and related topographic effect will be examined from a kinematic viewpoint in connection with the characteristic velocity in the following subsections for two different cases of upper-layer geostrophic wind: $(u_1, v_1)=(1, 1)$ in case 1, and $(u_1, v_1)=(1, -1)$ in case 2.

4.2.1. Case 1. The characteristic velocity fields are plotted in (ξ, y) space in Figs. 2a–c where the parameters used are $R=1$, $\gamma=0.5$ and $(u_1, v_1)=(1, 1)$. As functions of ξ and y, u_o and v_o are not explicitly dependent on time t in (ξ, y) space, but $\xi(y, t)$ is a function of time in physical space. By superimposing the isochrones of the surface front (Fig. 3a) on the vector field of (u_o, v_o) in Fig. 2c, one can see how the characteristic velocity (u_o, v_o) changes with time as the surface front moves in physical space. The v_o field in Fig. 2b is symmetric with respect to the ξ-axis and has a maximum on the west side and a minimum on the east side of the mountain. This distribution of v_o can be explained by the second term in (3.9b) that represents the topographic effect on v_o.

Fig. 2a shows that the u_o field is not symmetric. This asymmetry is a mesoscale feature, because it

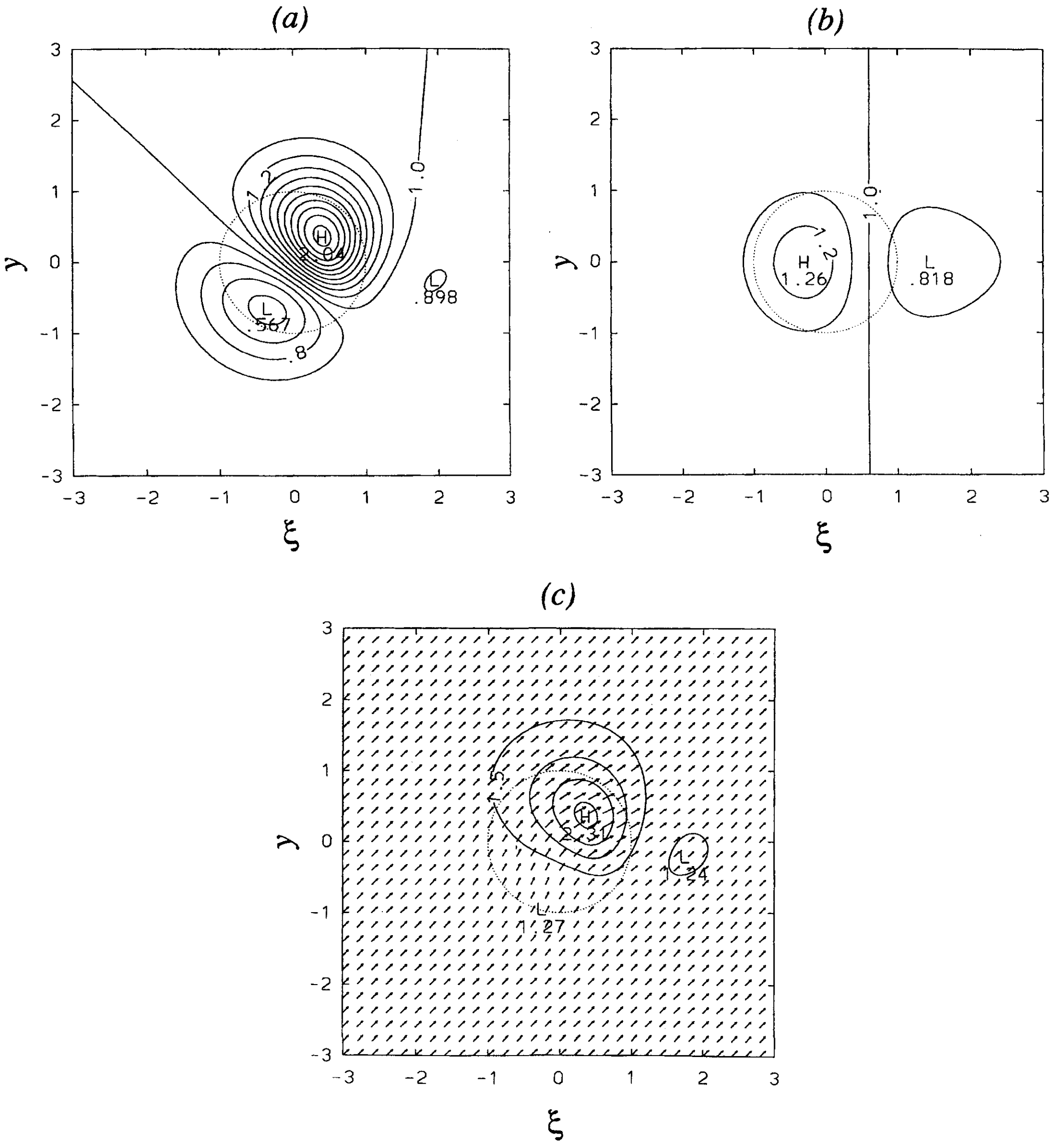

Fig. 2. Component and vector fields of the characteristic velocity (u_o, v_o) plotted in (ξ, y) space for case 1 ($R=1$, $\gamma=0.5$, $u_1=1$, and $v_1=1$): (a) u_o field; (b) v_o field; (c) (u_o, v_o) vectors and $|(u_o, v_o)|$ field. Contour increment is 0.1 in (a) and (b), and 0.25 in (c). The vector scale in (c) can be inferred from the fact that $(u_o, v_o)=(1, 1)$ far away from the mountain. The dotted circle shows the e-folding height contour of the mountain.

vanishes in the limit of small R, as shown by the following $O(R^2)$ truncation of (3.10b):

$$u_0 = \frac{[u_1 - R\partial h_o/\partial y + R^2(1-v_1)\partial^2 h_o/\partial x \partial y]_\xi}{[1+R^2\partial^2 h_o/\partial x^2]_\xi}. \tag{4.7}$$

Eq. (4.7) is obtained under the condition of small R. For $(u_1, v_1)=(1, 1)$, the third term vanishes in the numerator of (4.7). The second term in the numerator describes a pattern that is symmetric about the y-axis and antisymmetric about the ξ-axis, while the second term in the denominator of

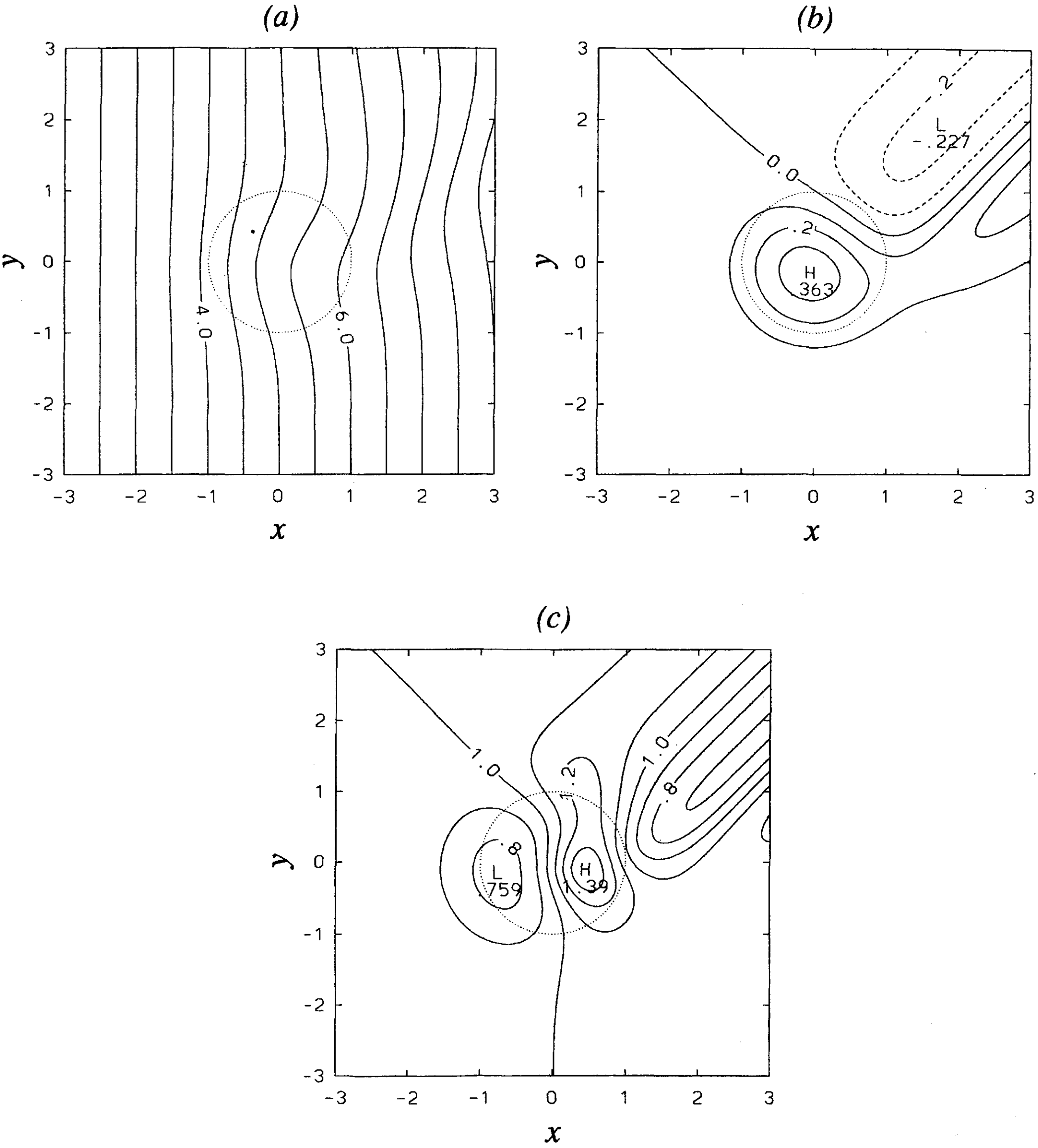

Fig. 3. Frontal movement in the dimensionless (x, y) space for case 1: (a) Isochrones of the surface front with dimensionless time interval 0.5; (b) Time shift caused by the mountain for the front to reach the concerned location; (c) Frontal local speed computed from (4.10). The front is initially straight and located at $x=-5$. Contour increment is 0.1 in (b) and (c). The dotted circle shows the mountain as in Fig. 2.

(4.7) describes a pattern that is symmetric about both y-axis and ξ-axis. The combination of the numerator and denominator in (4.7) describes a pattern that is symmetric about the y-axis. For the solutions obtained here with $R=1$ and $\gamma=0.5$, the truncation error of (4.7) is actually as large as $O(R^3\gamma)=O(\gamma)$. Thus, (4.7) explains only a part of the u_o field in Fig. 2a, although it does show that the asymmetry in Fig. 2a is due to the mesoscale dynamics.

Fig. 2c shows that the vector field (u_o, v_o) contains an anticyclonic rotation induced by the mountain. This anticyclonic rotation may be demonstrated partially by the O(R) truncation of (4.7) and (3.9b) with $R \ll O(1)$:

$$u_o = u_1 - R[\partial h_o/\partial y]_\xi, \tag{4.8a}$$

$$v_o = u_1 + R[\partial h_o/\partial x]_\xi. \tag{4.8b}$$

The truncated characteristic velocity (u_o, v_o) consists of two parts: the constant part (u_1, v_1), and the topographic part $R[-\partial h_o/\partial y, \partial h_o/\partial x]_\xi$. The second part is an anticyclonic vector field showing how the surface front is distorted by the mountain to O(R). Again, since the solution is obtained with $R=1$ and $\gamma=0.5$, the truncation errors of (4.8a,b) are actually as large as $O(R^2\gamma)=O(\gamma)$. As will be further discussed in Subsection 4.3, the anticyclonic rotation can be explained by the conservation of potential vorticity of the cold frontal flow over the mountain ridge.

Shown in Fig. 3a are the isochrones of the surface front which is initially straight and located at $x=-5$. The numerical value on the solid lines represents the time by which the front is located. The surface front is distorted in the mountain area. After the surface front passes the mountain, the distorted front becomes nearly stationary to the upper-layer wind, indicating that the effect of the mountain on the surface front movement is significantly reduced and the characteristics are quite similar to those described by the solutions in the absence of topography in the Appendix. Fig. 3b shows the time shift caused by the mountain for the front to reach the concerned location in comparison with the time needed for the front to reach the same location without the mountain. As an integral measure of frontal acceleration/deceleration, this time shift is similar to the frontal displacement caused by topography in Bannon (1984). Positive time shift means that the front is displaced backward by the mountain, while negative time shift means that the front is displaced forward by the mountain. As shown in Fig. 3b, the front is displaced backward over the major part of the mountain, with the maximum time shift approximately coinciding with the peak of the mountain. Negative time shift is found to the north and northeast of the mountain peak. Downstream of the mountain and south of the above negative time shift area is another region of positive time shift. The banded negative and positive areas downstream to the northeast of the mountain are caused by the translation of the distorted front.

In a synoptician's weather map, frontal propagation speed is often measured locally in the direction normal to the surface front. We denote by $\boldsymbol{n}$ the local unit vector normal to the surface front, and by n the local coordinate in this direction. By definition, $\boldsymbol{n}=(1, -\partial\xi/\partial y)/[1+(\partial\xi/\partial y)^2]^{1/2}$. For a given time interval Δt, the local displacement of the front is given by

$$\Delta n = \Delta\xi/[1+(\partial\xi/\partial y)^2]^{1/2}, \tag{4.9}$$

where $\Delta\xi=\xi(y, t+\Delta t)-\xi(y, t)$ is the frontal displacement in the x-direction during the time interval of Δt. The frontal local speed is then given by

$$\partial n/\partial t = (\partial\xi/\partial t)/[1+(\partial\xi/\partial y)^2]^{1/2}. \tag{4.10}$$

Here, $\partial\xi/\partial t$ is the frontal speed measured in the x-direction. Clearly, for a straight front along the y-direction, $\partial\xi/\partial y=0$ and hence $\partial n/\partial t=\partial\xi/\partial t$. For curved fronts, however, $|\partial n/\partial t|<|\partial\xi/\partial t|$ in general. Substituting $\partial\xi/\partial t$ from (3.8) into (4.10) and making use of the definition of $\boldsymbol{n}$, we further obtain

$$\partial n/\partial t = (u_o, v_o)\cdot\boldsymbol{n}. \tag{4.11}$$

As shown in Fig. 3c, the frontal local speed reaches minimum on the western slope and maximum on the eastern slope of the mountain, indicating that the front is locally decelerated while climbing up the ridge and accelerated when running down the hill.

4.2.2. Case 2. The parameters used here are the same as in case 1 except that v_1 is changed from 1 to -1. The topographic effect on the v_o field is represented by the second term in (3.9b) and is independent of v_1, so the v_o field is affected by the mountain in the same way in this case as in case 1. Therefore, the v_o field (figure not shown) is the same as that in case 1 (Fig. 2b) except for a constant value of -2. The topographic effect on the u_o field is not independent of v_o or v_1 as shown in (3.10b). According to (4.7), the u_o field is affected by v_1 on $O(R^2\gamma)$.

The 3rd term in the numerator of (4.7) is a cross-derivative term and can cause an asymmetric feature in the u_o field. This cross-derivative term vanishes in case 1 ($v_1=1$) but not in case 2 ($v_1=-1$), so the asymmetry in the u_o field is a feature of $O(R^3\gamma)$ in case 1 and is a feature of $O(R^2\gamma)$ in case 2. This may partially explain why u_o field in Fig. 4a is very different from that in Fig. 2a. Fig. 4b shows that the vector field (u_o, v_o) contains an anticyclonic rotation. This anticyclonic rotation can be explained partially by (4.8) as in case 1.

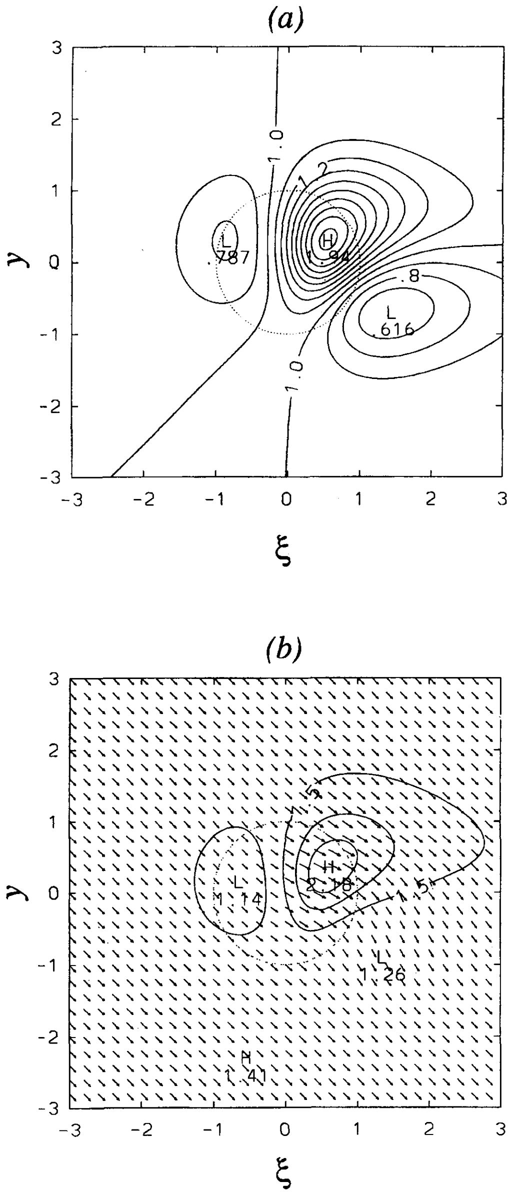

Fig. 4. As in Fig. 2, but for case 2 ($R=1$, $\gamma=0.5$, $u_1=1$, and $v_1=-1$): (a) u_o field; (b) (u_o, v_o) vectors and $|(u_o, v_o)|$ field.

The surface frontal movement is shown by the isochrones in Fig. 5a. The front is distorted by the mountain more severely in this case than in case 1 (Fig. 3a). After the front passes the mountain, the bulged part of the distorted front expands southward. This is different from that in case 1. The banded positive area in Fig. 5b indicates that the front is displaced forward more persistently following the upper-layer geostrophic wind in this case than in case 1. Fig. 5c shows that the frontal local speed is positive on the eastern slope of the mountain and significantly larger in this case than in case 1 (Fig. 3c).

4.3. *Geostrophic and ageostrophic winds*

To understand the dynamic aspect of the frontal movement and related topographic modification of the front, the frontal motion needs to be analyzed in connection with the geostrophic and ageostrophic components of the perturbation wind field. The related problems are examined in the following subsections for the same two cases as in Subsections 4.2.1 and 4.2.2. To facilitate the analysis, the lower-layer total wind is partitioned as follows: $(u, v)=(u_1, v_1)+(u', v')=(u_1, v_1)+(u_g', v_g')+(u_a, v_a)$, where (u', v') is the perturbation wind, $(u_g', v_g')=(-R\partial h/\partial y, R\partial h/\partial x)$ is the perturbation geostrophic wind, and $(u_a, v_a)=(u_a, 0)$ is the ageostrophic wind with $v_a\equiv 0$ as assumed in (2.1)–(2.3).

4.3.1. *Case 1.* The vector field of the perturbation wind (u', v') at $t=5$ is shown in Fig. 6a, where contours are plotted for the zonal ageostrophic wind u_a. The height field h is shown in Fig. 6b, from which the perturbation geostrophic wind can be inferred by using $(u_g', v_g')=(-R\partial h/\partial y, R\partial h/\partial x)$. Clearly, there is no perturbation wind on the warm side of the surface front, and the northerly jet-like perturbation wind behind the front is geostrophically balanced with the frontal slope (that is, $v'=R\partial h/\partial x$ as in (2.1)). The height field in Fig. 6b suggests that the perturbation geostrophic flow is curved anticyclonically over the mountain. This anticyclonic flow curvature can be explained by the conservation of potential vorticity of the shallow frontal flow over the mountain (see eq. (2.4)). The perturbation geostrophic wind

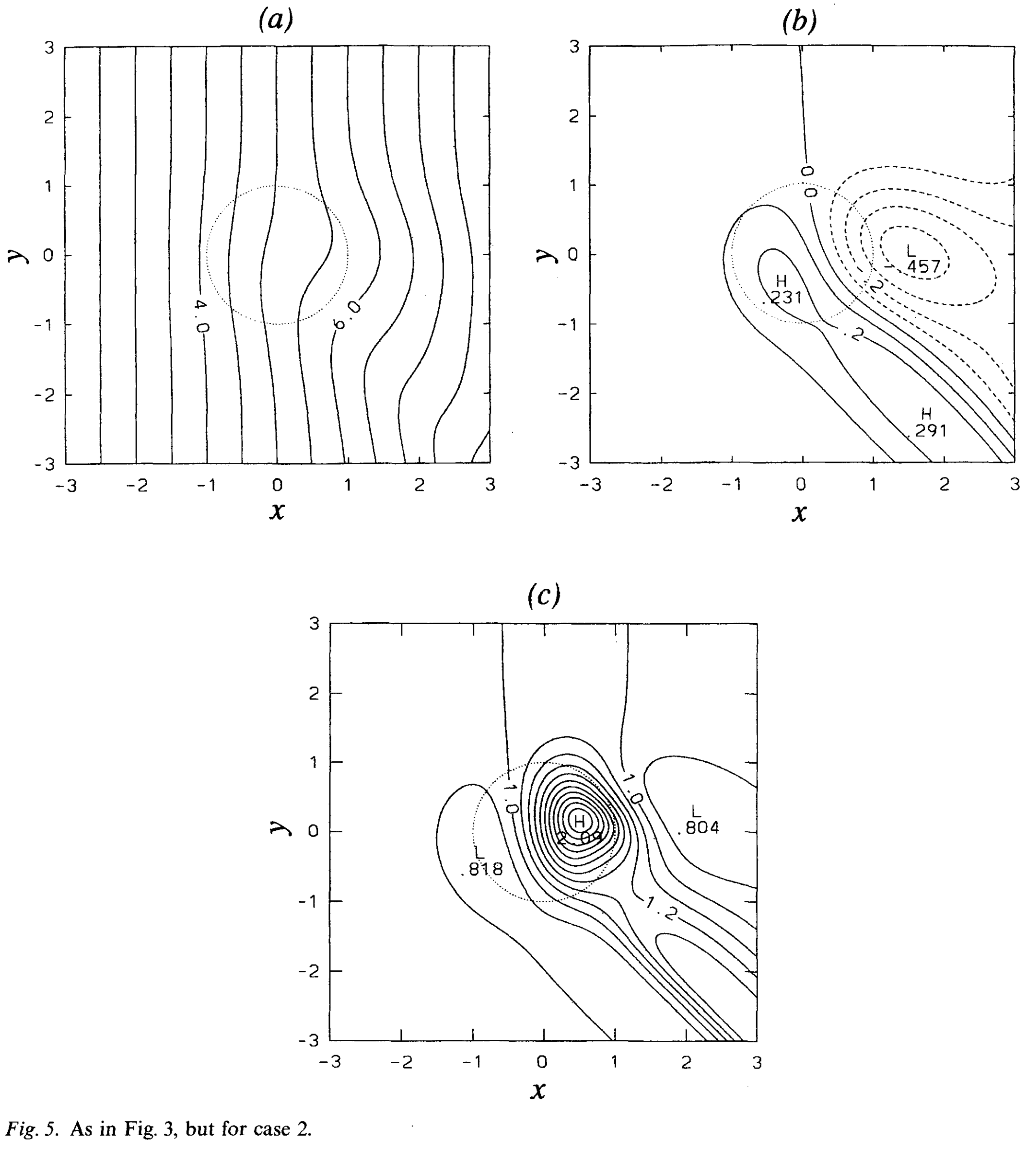

Fig. 5. As in Fig. 3, but for case 2.

intersects the distorted surface front and, thus, affects the propagation of the wave pattern of the distorted front.

By rewriting (2.2) into $R\mathrm{d}v/\mathrm{d}t = -u_{\mathrm{a}} \equiv -(u' - u_{\mathrm{g}}')$, we can see that $-u_{\mathrm{a}}$ represents the imbalance between the perturbation Coriolis force (represented by $-u'$) and perturbation pressure gradient force (represented by $-u_{\mathrm{g}}' = R\partial h/\partial y$) in the y-direction. This force imbalance accelerates the total flow in the y-direction and tends to produce a southerly mountain-barrier jet in the negative u_{a} area — the area prone to cold-air damming on the upstream side of the mountain (Xu, 1990; Xu et al., 1996). Since $v = v_1 + v'$ and v_1 is constant, we have $\mathrm{d}v/\mathrm{d}t = \mathrm{d}v'/\mathrm{d}t$. By applying the above force analysis to $R\mathrm{d}v'/\mathrm{d}t = -u_{\mathrm{a}}$ and noting that $v' < 0$, one can understand why the northerly component of the perturbation wind decreases in

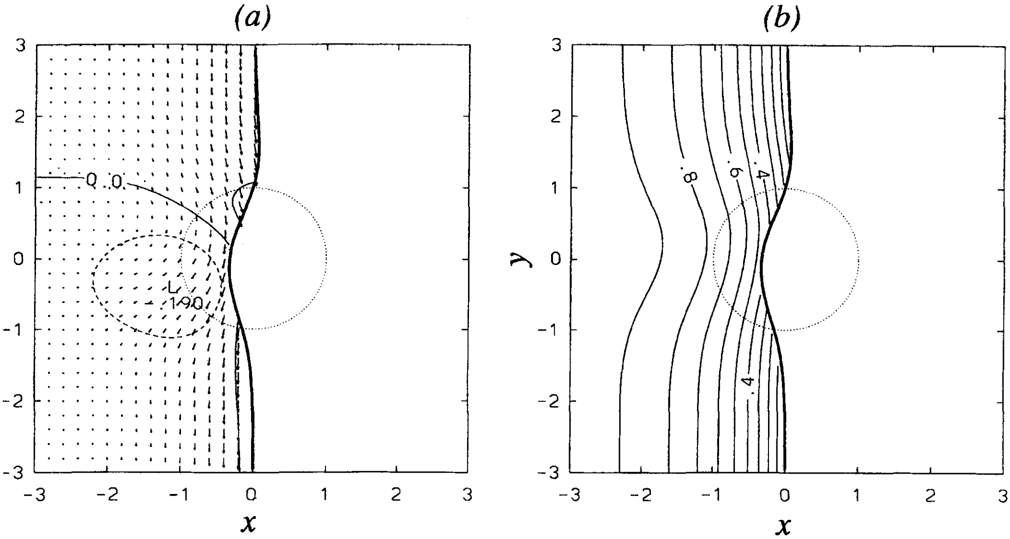

Fig. 6. (a) Perturbation wind vector (u', v') and the zonal ageostrophic wind u_a (contour increment is 0.1 with solid lines for positive and dashed lines for negative values), and (b) height field h (contour increment is 0.1) in (x, y) space at $t=5$ for case 1. The vector scale can be inferred from the fact that $(u', v') \to (0, -1)$ as $|y| \to \infty$ along the surface front (shown by the thick curve). The dotted circle shows the mountain as in Fig. 2.

the negative u_a area but increases in the positive u_a area, as shown in Fig. 6a.

The surface front can be distorted only if (u', v') intersects the front. The distorted part will grow locally if the along-front distribution of the front-normal component of (u', v') is in phase with respect to the wave pattern of the front, and will propagate along the front if the along-front distribution of the front-normal component of (u', v') is 90° out of phase with respect to the wave pattern of the front. In Fig. 6a, the along-front distribution of the front-normal component of (u', v') is slightly less than 90° out of phase with respect to the wave pattern of the distorted front, suggesting that the wave pattern grows very slowly while propagating southward along the front relative to the upper-layer geostrophic wind (Fig. 3a). Note further that the along-front distribution of the front-normal component of (u_g', v_g') is nearly 90° out of phase with respect to the wave pattern of the distorted front (Fig. 6b), while the along-front distribution of u_a is significantly less than 90° out of phase with respect to the wave pattern (Fig. 6a). Thus, the along-front propagation of the wave pattern is caused mainly by the perturbation geostrophic wind, while the growth of the wave pattern is caused mainly by the ageostrophic wind at this time (i.e., $t=5$).

Fig. 7a shows that by $t=6$ a northwesterly jet-like flow is formed in the perturbation wind field on the northern slope of the mountain. A similar jet-like flow exists in the geostrophic perturbation wind field, as shown by the height field in Fig. 7b. The u-component of this jet-like flow is enhanced by the ageostrophic wind as shown by the positive contours in Fig. 7a. Since u_a is strongly positive in the jet-like flow area, the imbalance between the Coriolis force and pressure gradient force is strong in the y-direction and accelerates the flow southward. This explains why the northwesterly jet-like flow is enhanced in Fig. 7a as the surface front moves down to the lee side of the mountain.

In Fig. 7a, the along-front distribution of u_a is almost completely out of phase (by 180°) with respect to the wave pattern of the distorted front, suggesting that the ageostrophic wind causes the wave pattern to decay at $t=6$. The along-front distribution of the front-normal component of (u_g', v_g') is 90° out of phase with respect to the wave pattern of the distorted front in Fig. 7b, so the perturbation geostrophic wind still causes the wave pattern to propagate southward along the

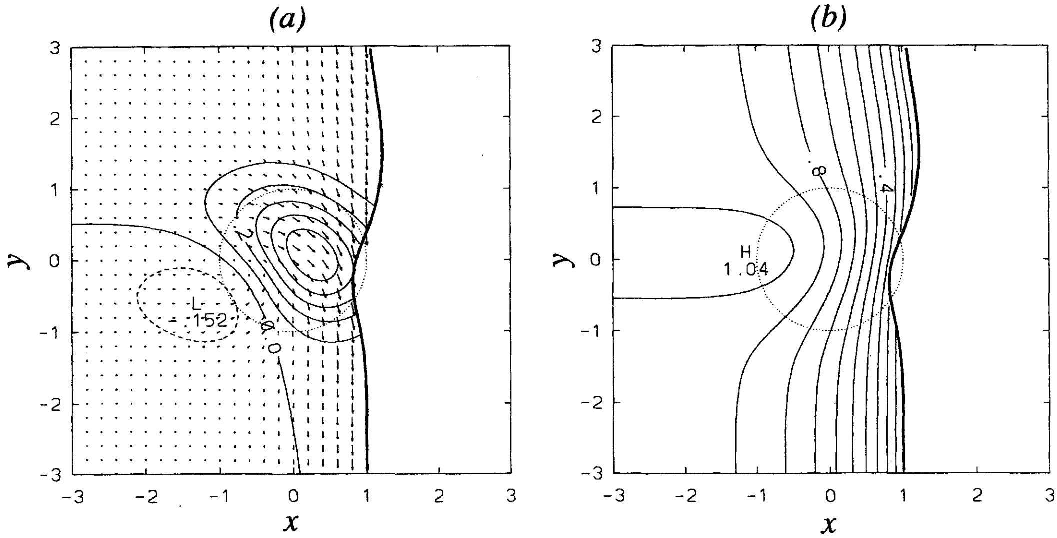

Fig. 7. As in Fig. 6, but for the results at $t=6$.

front relative to the upper-layer geostrophic flow at this time.

4.3.2. Case 2. The upper-layer geostrophic wind is northwesterly in this case, and the lower-layer total wind is enhanced by the strong northerly perturbation wind behind the front. As the front moves onto the mountain (say, at $t=5$), this northerly component flow is decelerated ($-\mathrm{d}v/\mathrm{d}t<0$) on the northwestern slope but is accelerated ($-\mathrm{d}v/\mathrm{d}t>0$) on the southwestern slope of the mountain. Consequently, the along-front distribution of u_a ($=-R\mathrm{d}v/\mathrm{d}t$) in this case (Fig. 8a) is stronger than and opposite to that in case 1 (Fig. 6a).

The along-front distribution of u_a in Fig. 8a is more than $-90°$ out of phase with respect to the wave pattern of the distorted front, so the ageostrophic wind tends to cause the wave pattern to slowly decay and propagate northward along the front at this time ($t=5$). Fig. 8b shows that the front-normal component of the perturbation geostrophic wind is stronger than in case 1 (Fig. 6b), and its along-front distribution is similar to that in case 1 but less than 90° out of phase with respect to the wave pattern of the distorted front. Thus, the perturbation geostrophic wind tends to cause the wave pattern to grow and propagate southward along the front at this time ($t=5$).

Since u_g' and u_a have opposite signs along the front, the front-normal component of the perturbation wind u' is much weaker than that in case 1 and its along-front distribution is nearly in phase with the wave pattern of the distorted front, as shown in Fig. 8a. Thus, the southward propagation of the wave pattern caused by the perturbation geostrophic wind is largely offset by the northward propagation caused by the ageostrophic wind, but the growth caused by the perturbation geostrophic wind is a dominant feature.

Fig. 9a shows that an anticyclonically curved perturbation flow is formed on the eastern slope of the mountain by $t=6$. A similar feature exists in the perturbation geostrophic wind field as shown by the height field in Fig. 9b. The curved flow is enhanced by the strong westerly ageostrophic wind on the northeastern slope and by the strong easterly ageostrophic wind on the southeastern slope of the mountain (shown by contours in Fig. 9a). The strong westerly ageostrophic wind on the northeastern slope implies that the northerly flow component is accelerated, while the strong easterly ageostrophic wind on the southeastern slope implies that the northerly flow component is decelerated by the imbalance between the Coriolis force and pressure gradient force.

The along-front distribution of u_a in Fig. 9a is

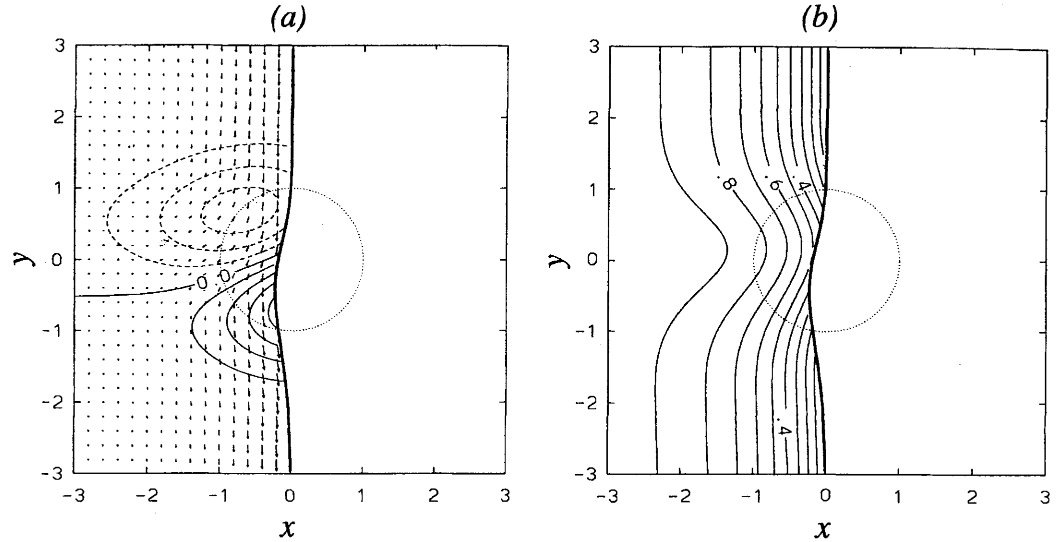

Fig. 8. As in Fig. 6, but for case 2.

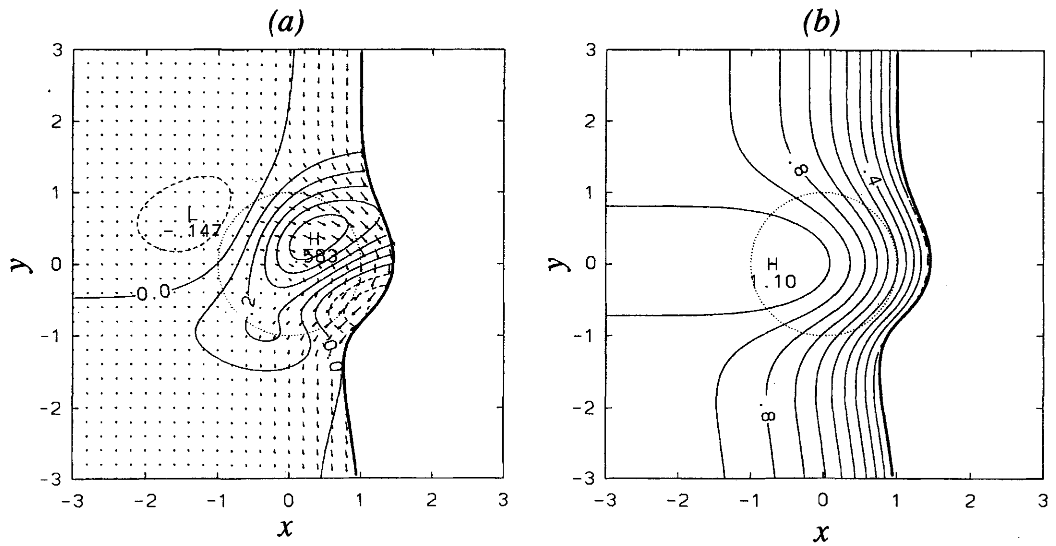

Fig. 9. As in Fig. 7, but for case 2.

nearly 90° out of phase with respect to the wave pattern of the bulged surface front, so it tends to cause the bulged pattern to propagate northward relative to the upper-layer flow. On the other hand, as shown in Fig. 9b, the perturbation geostrophic wind intersects the bulged front only on its southern part and thus tends to cause this part to move southward relative to the upper-layer flow. The combination of the above two component wind fields explains why the total perturbation flow nearly parallels the southern part but intersects the northern part of the bulged front, as shown in Fig. 9a, and why the bulged pattern expands as the front moves eastward (see Fig. 5a).

5. Concluding remarks

A two-layer semigeostrophic model is developed to study the movements of surface cold fronts over a quasi-two-dimensional mountain on an f-plane. This model can be considered as an extension of the two-dimensional model of Davies (1984). Analytical expressions are obtained for the lower-layer height and velocity fields in terms of the surface frontal position and topography, and a hyperbolic differential equation is derived for the movement of the surface front. This hyperbolic differential equation is cast into a set of coupled ordinary differential equations and thus integrated by following the characteristic velocity. It is shown that the movement of the surface front can be conveniently described by the characteristic velocity, although the latter is not the parcel velocity at the surface front.

The present model breaks down when the topographic slope becomes as steep as the frontal slope on the lee side of the mountain. In this case, the zonal component of the characteristic velocity becomes unbounded and the model's surface front is along the meridional direction at the point of breakdown. This breakdown condition is similar to that of Davies (1984). The unbounded characteristic velocity indicates unbounded parcel velocity at the front, which implies a very strong downslope wind on the lee side of the mountain caused by a fast geostrophic adjustment process beyond the description of the present model. For a given Gaussian-type mountain profile, the breakdown condition sets an upper limit or, say, critical value for the model's mountain height (scaled by the far-upstream depth of the lower-layer cold air). This critical height is independent of the upper-layer geostrophic flow and increases monotonically as the Rossby number decreases (see (4.6) and Fig. 1).

Solutions are obtained for flows over an isolated Gaussian-type mountain in the dimensionless space (scaled by the short semi-axis and long semi-axis of the e-folding height contour of the mountain in the x-direction and y-direction, respectively). These solutions are examined for two cases of different upper-layer geostrophic wind: southwesterly in case 1, and northwesterly in case 2. It is found that in both cases a jet-like northwesterly flow develops in the perturbation wind field on the northern slope of the mountain as the surface front passes the mountain. This feature represents a quasi-steady response to the mountain, and becomes more distinctive as the surface front moves further downstream to the east of the mountain. The jet-like northwesterly flow is enhanced by the westerly ageostrophic flow superimposed on the northern branch of an anticyclonic circulation of the geostrophic flow, while the anticyclonic geostrophic flow and its associated positive height anomaly are maintained by the conservation of potential vorticity for the shallow lower-layer flow over the mountain. This type of topography-induced strong wind phenomena has been observed in the real atmosphere (Colquhoun et al., 1985).

In the absence of topography, the front is advected by the upper-layer geostrophic wind and the frontal flow is purely geostrophic as shown in the Appendix. Therefore, the deviation from this behavior is the essential part showing the topographic effect on the frontal movement. Since this deviation can be expressed analytically in terms of the perturbation characteristic velocity obtained by subtracting the upper-layer geostrophic velocity from the characteristic velocity (see Sections 3 and 4.2), the topographic effect can be examined conveniently from a kinematic viewpoint in connection with the perturbation characteristic velocity. In terms of a small Rossby number expansion, the first-order perturbation characteristic velocity describes an anticyclonic circulation that follows the mountain's height contours (see (4.8)). This implies that the surface front experiences a clockwise deformation when it passes the mountain following the upper-layer geostrophic wind. This feature is seen in our model's solutions and also agrees qualitatively with the numerical results of Schumann (1987) and the analytical results of the quasi-geostrophic extension of Davies' model (1984) to three-dimensions by Blumen (1992). The higher-order terms of the characteristic velocity show that the meridional component of the characteristic velocity is independent of the upper-layer geostrophic wind and has a symmetric distribution with respect to the short axis of the mountain's height contours. The zonal component, however, is affected by the meridional component of the upper-layer geostrophic wind and has an asymmetric distribution purely due to the mesoscale dynamics.

The frontal evolution and related topographic modification are examined from a dynamic viewpoint in connection with the geostrophic and ageostrophic components of the perturbation wind field. Roughly, the frontal evolution can be divided into two stages: the upslope stage and the downslope stage. During the upslope stage, the surface front moves on the upstream side of the mountain, the cold air layer becomes shallower over the mountain, and the perturbation geostrophic flow is curved anticyclonically under the constraint of potential vorticity conservation. The curved perturbation geostrophic flow intersects the distorted surface front and tends to move the distorted frontal pattern southward (in both cases). This tendency is largely offset by the ageostrophic process in case 2 but not in case 1. Thus, the distorted frontal pattern propagates southward relative to the upper-layer geostrophic wind in case 1 but not in case 2. The slow growth of the distorted frontal pattern is caused mainly by the ageostrophic wind in case 1 but by the geostrophic wind in case 2. Features in the ageostrophic wind field are interpreted in terms of mountain-induced Lagrangian deceleration (or acceleration) of the geostrophic flow.

During the downslope stage, the surface front moves on the lee side of the mountain, the front becomes steep, and the perturbation geostrophic flow becomes strong and fairly parallel to the distorted front. The ageostrophic wind becomes strong in both cases but has very different distributions in the two cases. The combination of the geostrophic wind and ageostrophic wind causes the distorted frontal pattern to slightly decay in case 1 and causes the bulged pattern of the distorted front to expand in case 2. After the downslope stage, the surface front moves further downstream to the east of the mountain (see Figs. 3a, 5a), the perturbation geostrophic flow becomes nearly parallel to the front and the ageostrophic wind becomes very weak, and the distorted front becomes nearly stationary with respect to the upper-layer geostrophic wind in both cases. Overall, the characteristics of the front after the downslope stage are quite similar to those described by the solutions in the absence of topography in the Appendix. As the distorted front propagates far downstream, leaving behind an anticyclone permanently associated with the topography, the transient and long-term effects of the topography on the flow field are essentially decoupled.

In addition to the previously mentioned breakdown condition, the assumed quasi-two-dimensionality and semigeostrophy represent further limitations of the present model when it is applied to strongly curved flows around more realistic three-dimensional topography (Gent et al., 1994). Even with the quasi-two-dimensional topography, caution should be used when the model is applied to situations where surface fronts intersect the long axis of the topographic height contours at significant angles. Flows in these circumstances might be described in terms of balanced dynamics with certain intermediate models (McWilliams and Gent, 1980; Xu, 1994), but solutions of such models remain to be sought. Despite the restrictions mentioned above, however, the present analytical model provides useful insights into the dynamical effects of a quasi-two-dimensional mountain ridge on the movements of cold fronts that are nearly parallel to the mountain ridge and impinge upon the mountain ridge in a nearly normal direction.

6. Acknowledgements

We are grateful to Dr. Brian Fiedler, Dr. Paul J. Kushner, and the two anonymous reviewers for their helpful comments. Numerical calculations were performed on the Cray Y-MP C90 at the Pittsburgh Supercomputing Center and on the IBM RS/6000 cluster at the Center for Analysis and Prediction of Storms (CAPS), University of Oklahoma. This work was supported by the National Science Foundation under Grant ATM91–20009 at CAPS and Grant ATM-9417304 at CIMMS, University of Oklahoma, and by the Office of Naval Research (ONR), Program Element 0602435N to the Marine Meteorology Division of the Naval Research Laboratory at Monterey.

7. Appendix

Solutions in the absence of topography

In the case of $h_o = 0$ and constant u_1 and v_1, (3.10b) and (3.9b) reduce to $u_o = u_1$ and $v_o = v_1$, respectively. If the surface front is initially described by $\xi = \xi_o(y)$, where $\xi_o(y)$ is a given function of y, (3.8) has a solution of ξ in the following form

$$\xi(y,t)=\xi_o(y-v_1t)+u_1t. \quad \text{(A1)}$$

Here, (A1) shows that the surface front translates at the speed of u_1 in the x-direction, while its initial pattern given by ξ_o shifts in the y-direction at a speed of v_1. According to (2.8b), $D=1$ in the absence of topography, so (2.10) reduces to:

$$h=1-e^{(x-\xi)/R}. \quad \text{(A2)}$$

With h given in (A2), it is easy to verify the following relations

$$u=u_g=u_1-(\partial\xi/\partial y)e^{(x-\xi)/R}, \quad \text{(A3)}$$

that is, the frontal motion is purely geostrophic if there is no topographic effect.

REFERENCES

Baines, P. G. 1980. The dynamics of the southerly buster. *Aust. Meteor. Mag.* **28**, 175–200.

Bannon, P. R. 1984. A semigeostrophic model of frontogenesis over topography. *Beitr. Phys. Atmos.* **57**, 393–408.

Blumen, W. 1992. Propagation of fronts and frontogenesis versus frontolysis over orography. *Meteorol. Atmos. Phys.* **48**, 37–50.

Blumen, W. and Gross, B. D. 1987. Semi-geostrophic flow over orography in a stratified rotating atmosphere. Part I: Steady three-dimensional solutions over finite ridges. *J. Atmos. Sci.* **44**, 3007–3019.

Buzzi, A. and Tibaldi, S. 1978. Cyclogenesis in the lee of the Alps: a case study. *Quart. J. Roy. Meteor. Soc.* **104**, 271–287.

Colquhoun, J. R., Shepherd, D. J., Coulman, C. E., Smith, R. K. and McInnes. K. 1985. The southerly burster of south eastern Australia: an orographically forced cold front. *Mon. Wea. Rev.* **113**, 2090–2107.

Davies, H. C. 1984. On the orographic retardation of a cold front. *Beitr. Phys. Atmos.* **57**, 409–418.

Davies, H. C. 1986. Diagnostic studies of meso-α scale flow on the Alpine northside. *Scientific Results of the Alpine Experiment (ALPEX)*, GARP Publication Ser. 27, WMO/TD-No. 108, Vol. II, p. 425–436.

Egger, J. and Hoinka, K. P. 1992. Fronts and orography. *Meteorol. Atmos. Phys.* **48**, 3–36.

Egger, J. and Hatt, H. 1994. Passage of a frontal zone over a two-dimensional ridge. *Q. J. R. Meteorol. Soc.* **120**, 557–572.

Garrat, J. R., Howells, P. A. C. and Kowalczyk, E. 1989. The behavior of dry fronts traveling along a coastline. *Mon. Wea. Rev.* **117**, 1208–1220.

Gent, P. R., McWilliams, J. C. and Snyder, C. 1994. Scaling analysis of curved fronts: validity of the balanced equations and semigeostrophy. *J. Atmos. Sci.* **51**, 160–163.

Gu, W. and Wu, R. 1992. Theoretical study of the influence of topography on the cold frontal motion. *Advances in Atmos. Sci.* **9**, 167–172.

Hoinka, K. P. 1986. On the diagnosis of a cold front observed during ALPEX. *Scientific Results of the Alpine Experiment (ALPEX)*, GARP Publication Ser. 27, WMO/TD-No. 108, Vol. II, 444–453.

Hoinka, K. P. and Heimann, D. 1988. Orographic channeling of a cold front by the Pyrenees. *Mon. Wea. Rev.* **116**, 1817–1823.

Hoskins, B. J. and Bretherton, F. P. 1972. Atmospheric frontogenesis models: mathematical formulation and solution. *J. Atmos. Sci.* **34**, 1859–1867.

McWilliams, J. C. and Gent, P. R. 1980. Intermediate models of planetary circulations in the atmosphere and ocean. *J. Atmos. Sci.* **37**, 1657–1678.

Schumann, U. 1987. Influence of mesoscale orography on idealized cold fronts. *J. Atmos. Sci.* **44**, 3423–3441.

Smith, R. B. 1986. Mesoscale meteorology in the Alps. *Scientific Results of the Alpine Experiment (ALPEX)*, GARP Publ. Ser. 27, WMO/TD-No. 108, Vol. II, 407–423.

Steinacker, R. 1981. Analysis of the temperature and wind fields in the Alpine region. *Geophys. Astrophys. Fluid Dyn.* **17**, 51-62.

Steinacker, R. 1983. The first ALPEX-SOP cold front on 2 March 1982. *ALPEX preliminary scientific results*, WMO Geneva, GARP-ALPEX No.7, p. 87–96.

Williams, R. T., Peng, M. S. and Zankofsky, D. A. 1992. Effects of topography on fronts. *J. Atmos. Sci.* **49**, 287–305.

Xu, Q. 1990. A theoretical study of cold air damming. *J. Atmos. Sci.* **47**, 2969–2985.

Xu, Q. 1994. Semi-balance model – Connection between geostrophic-type and balance-type intermediate models. *J. Atmos. Sci.* **51**, 953–970.

Xu, Q., Gao, S. and Fiedler, B. H. 1996. A theoretical study of cold air damming caused by upstream blocking of stratified flow. *J. Atmos. Sci.* **53**, 312–326.